

RESEARCH

Open Access



# Full degree-of-freedom polarization hologram by freeform exposure and inkjet printing

Jianghao Xiong<sup>1,2\*</sup>, Haizheng Zhong<sup>3</sup>, Dewen Cheng<sup>1\*</sup>, Shin-Tson Wu<sup>2</sup> and Yongtian Wang<sup>1\*</sup>

\*Correspondence:

jhxiong@bit.edu.cn; cdwxk@bit.edu.cn; wyt@bit.edu.cn

<sup>1</sup> Beijing Engineering Research Center of Mixed Reality and Advanced Display, School of Optics and Photonics, Beijing Institute of Technology, Beijing, China

<sup>2</sup> College of Optics and Photonics, University of Central Florida, Orlando, FL 32816, USA

<sup>3</sup> MIIT Key Laboratory for Low-Dimensional Quantum Structure and Devices, School of Materials Science & Engineering, Beijing Institute of Technology, Beijing, China

## Abstract

Since the invention of holography by Dennis Gabor, the fabrication of holograms has mainly relied on direct recording of wavefront by engraving the intensity fringes of interfering electric fields into the holographic material. The degree-of-freedom (DoF) is often limited, especially for its usage as a holographic optical element in imaging or display systems, as what is recorded is what to use. In this work, based on the emerging self-assembled photo-aligned liquid crystal, a polarization hologram with full DoF for local manipulation of optical structure is demonstrated. The ability to record an arbitrary wavefront (in-plane DoF) is achieved by freeform surface exposure, while the local adjustment of deposited liquid crystal (out-of-plane DoF) is realized by inkjet printing. The methodology for designing and fabricating such a hologram is exemplified by building a full-color retinal scanning display without color crosstalk. Here, the arbitrary wavefront modulation capability helps to eliminate the aberrations caused by mismatched exposure and display wavelengths. The local liquid crystal adjustment ability enables the suppression of crosstalk by variation of chiral pitch and film thickness to tune the peak and valley of Bragg diffraction band. The demonstrated method is expected to greatly impact the fields of advanced imaging and display, such as augmented reality and virtual reality, that require optics with an ultrathin form factor and high degrees of design freedom simultaneously.

## Introduction

Holography is a method to record the wavefront information of a light beam into a medium, which can later be recovered by illuminating the medium (hologram) with a reference beam [1]. Traditional materials to record holograms mainly include silver halide emulsion [2], dichromated gelatin [3], photoresist [4], photorefractive materials [5] and photopolymer [6]. Although varied in detailed mechanisms, they generally rely on recording the spatially distributed intensity fringes of interfered beams with certain intensity-sensitive attributes of materials. In practical applications, photopolymer exhibits advantages over other materials because it does not require the sophisticated chemical developing process and is more stable [7]. Therefore, it has been widely used in holographic data storage, imaging, and displays [8]. However, the refractive index

modulation of photopolymer is typically in the order of 0.05, which may not be enough for certain applications like augmented reality (AR) and virtual reality (VR) displays. Additionally, its degree-of-freedom is limited because the volume refractive index distribution is determined in the recording process and cannot be adjusted afterwards.

From the perspective of optical diffraction, a hologram consists of the two-dimensional (2D) wavefront and volume structure. The 2D wavefront, corresponding to the in-plane degree-of-freedom, determines the distribution of  $k$ -vector and thus the directions of diffraction orders in local gratings. The volume structure, manifesting the out-of-plane degree-of-freedom, regulates the diffraction behaviors of local grating, such as diffraction efficiency and polarization response of all diffraction orders. For the holographic materials mentioned above, the wavefront and volume structure are usually formed simultaneously in the recording step by the three-dimensional intensity fringe distribution.

In contrast to previous intensity-sensitive recording methods, photoalignment technique relies on polarization state of light to induce the change of molecular order in recording material [9]. This non-contact alignment method has been widely applied in liquid crystal display industry to produce high-quality multi-domain alignment [10]. Recently, a new type of polarization hologram based on photo-aligned self-assembly liquid crystal [11] has been discovered. Unlike traditional holograms that record the 2D wavefront and volume fringes in a single exposure step, this type of liquid crystal polarization hologram (LCPH) records the 2D wavefront information in a thin ( $\sim 10$  nm) photoalignment layer without diffraction behavior. The volume structure responsible for optical diffraction is formed by the self-assembly liquid crystal deposited atop. Transmissive LCPHs based on geometric phase (or Pancharatnam-Berry phase) have been discovered and thoroughly studied in the 2000s [12, 13]. They generally exhibit a small diffraction angle due to the liquid crystal alignment issue in short-period devices [13]. On the contrary, reflective LCPHs have not been realized until recently. In the pioneering work of Ozaki et al. [14], a reflective device with a large transverse grating pitch ( $\sim 100$   $\mu\text{m}$ ) is demonstrated. The planar-aligned chiral liquid crystal (CLC) rotates along the bottom photo-aligned layer. The phase of Bragg-reflected light produced by the overall rotation of chiral structure is similar to the Pancharatnam-Berry phase in transmissive devices, and is therefore called Bragg-Berry phase [15]. However, when the transverse grating pitch is decreased to wavelength scale ( $< 1$   $\mu\text{m}$ ), it is found that the planar chiral structure no longer satisfies the lowest free energy condition. Instead, the liquid crystal directors would follow a slanted helical structure to maintain the low volume free energy and match the  $k$ -vector of bottom periodic pattern [16, 17]. Due to advantages like large diffraction angle, large refractive index modulation ( $\sim 0.2$ ), polarization sensitivity and dynamic tunability, this type of small-pitch polarization hologram has thereafter stirred up a new round of excitement for AR and VR displays applications [11].

Nonetheless, all previous works with LCPH are limited in the modulation abilities of wavefront and liquid crystal layer. Such a wavefront modulation capability is limited due to either the use of ordinary optical elements or the low patterning resolution of the employed spatial light modulator [18] ( $\sim 2$   $\mu\text{m}$ ) or laser writing [19] ( $\sim 400$  nm) where a resolution of  $\sim 50$  nm is required for a continuous short-period ( $\sim 500$  nm) pattern. To

produce a uniform liquid crystal layer, spin-coating (for liquid crystal monomer) or cell-formation (for fluidic liquid crystal) are commonly used. However, such a simple fabrication flow can no longer meet the demanding requirement of AR and VR imaging performance.

In this paper, we demonstrate a novel polarization hologram that manifests the complete manipulation degree-of-freedom in local hologram attributes. The arbitrary wavefront recording ability is achieved by freeform surface exposure, while the inkjet-printed liquid crystal is adopted to further adjust the post-exposure hologram's local properties like Bragg slant angle, thickness, birefringence, and so forth. To clearly illustrate our methodology, we pick an application scenario to build a full-color retinal scanning display without color crosstalk. In this application, the freeform surface is optimized to eliminate the aberrations of off-axis diffractive lenses produced by the mismatching between recording and display laser wavelengths. The inkjet-printed liquid crystal layer exhibits local modulations of chiral pitch and thickness that precisely control the peak and valley positions of the Bragg diffraction band. The crosstalk is eliminated by matching the targeted display wavelength with the peak and two other wavelengths with the valleys.

The potential applications of our proposed full-freedom polarization hologram extend far beyond the demonstrated one. For instance, by printing multiple layers of CLC with varying pitches, a diffractive optical element with diffraction bandwidth covering the whole visible spectrum can be fabricated, which has the potential of achieving pure-diffractive-element imaging in the visible. Or, by varying the local grating properties like thickness and chiral concentration, a polarization grating-based waveguide for AR displays can be designed and optimized for higher efficiency and better color uniformity. In essence, the full degree-of-freedom polarization hologram is applicable to any scenario requiring a compact thin-film diffractive optical element and high degree of design freedom simultaneously.

## Principle

Retinal scanning display (RSD) [20], also termed as virtual retinal display or Maxwellian display, is a type of display that scans modulated laser light directly onto the viewer's retina. The scanned light is usually focused into the viewer's eye pupil to avoid vignetting. For its application in AR, usually an off-axis reflective lens is adopted as the combiner. Diffractive optical elements (DOEs) are generally preferred over geometric half reflectors because they need not to be tilted and can maintain a glasses-like appearance.

Both photopolymer-based DOE and LCPH can be used as the combiner. The former has been widely applied in early pioneering researches of see-through RSD [21–23], while the latter has been recently adopted to achieve novel functions like dynamic pupil steering [24] and foveated display [25]. Previously demonstrated LCPH-based RSD systems only have the blue color channel because the azo-dye photoalignment material is only sensitive to blue recording lasers. Using the blue laser to record lens combiner for red and green would lead to aberrations that increase the size of focal spot, which impairs the long depth-of-focus attribute of RSD or even causes vignetting of field of view (FoV). The adoption of freeform surface for exposure can theoretically solve this problem by pre-correcting the aberrations in the freeform design process.

On the other hand, crosstalk is an important issue for DOE-based full-color RSDs. It originates from the fact that the diffraction efficiencies of DOE for the two wavelengths other than the desired one can hardly reach absolute zero across the whole lens aperture. This is due to the Bragg diffraction side bands, which is hard to control in photopolymer-based DOEs because the holograms are fixed after exposure. For LCPH, the control is possible if the local liquid crystal modulation can be achieved.

The working principle of our proposed full-freedom LCPH is illustrated in Fig. 1a. The arbitrary wavefront is achieved by freeform surface exposure, which corrects the associated aberrations for red, green and blue (RGB) display wavelengths. Locally adjusted liquid crystal film is realized by inkjet printing technique. The local adjustment of chiral concentration results in varied pitches of CLC's helical structure and therefore the slant angle of Bragg surface due to the self-assembly mechanism. Combined with the local thickness variation by controlling solution concentration, the Bragg diffraction band for local regions can be precisely controlled (Fig. 1b, c).

### Freeform surface design

In the past decade, freeform surfaces with a high degree-of-freedom have been widely applied in optical systems to significantly improve the imaging performance and reduce the system size [26]. Lately, freeform surfaces have been used to record photopolymer-type DOEs to improve the imaging performance in off-axis see-through

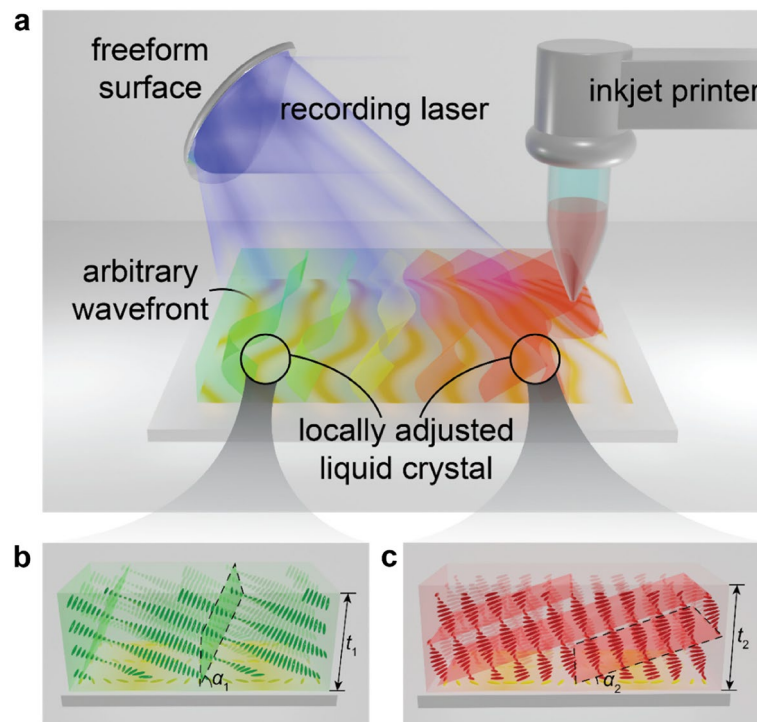


**Fig. 1** Schematics of full-freedom polarization hologram. **a** Realization of full-freedom polarization hologram by freeform surface exposure and inkjet printing. The yellow fringes on bottom correspond to the arbitrary wavefront achieved by regulating the recording laser with a freeform surface. The top layer with varied color signifies the locally adjusted liquid crystal film. **b** Left region with Bragg surface slant angle  $\alpha_1$  and thickness  $t_1$ . **c** Right region with Bragg surface slant angle  $\alpha_2$  and thickness  $t_2$

head-up display systems [27, 28]. The use of freeform surface to record LCPH is similar. But a main difference from its use in photopolymer-type DOEs is that only the 2D wavefront needs to be considered as the volume grating is formed by the self-assembled liquid crystal.

The following description is for the green DOE unless specified otherwise. The first step in freeform surface design is the determination of desired wavefront function  $\varphi(x, y)$  that regulates the local diffraction direction of light. The gradient of  $\varphi(x, y)$ ,  $\nabla\varphi$ , represents the local grating vector. The light is diffracted according to the grating equation:

$$\vec{k}_{out} = \vec{k}_{in} + \nabla\varphi \tag{1}$$

where  $\vec{k}_{in}$  and  $\vec{k}_{out}$  are  $k$ -vectors of input and output lights. The DOE wavefront function  $\varphi(x, y)$  should be designed according to the requirements of each specific optical system. In our case of RSD, the DOE serves as an off-axis lens that focuses the obliquely incident light onto a point (Fig. 2a). The wavefront function in this case has an analytical expression:

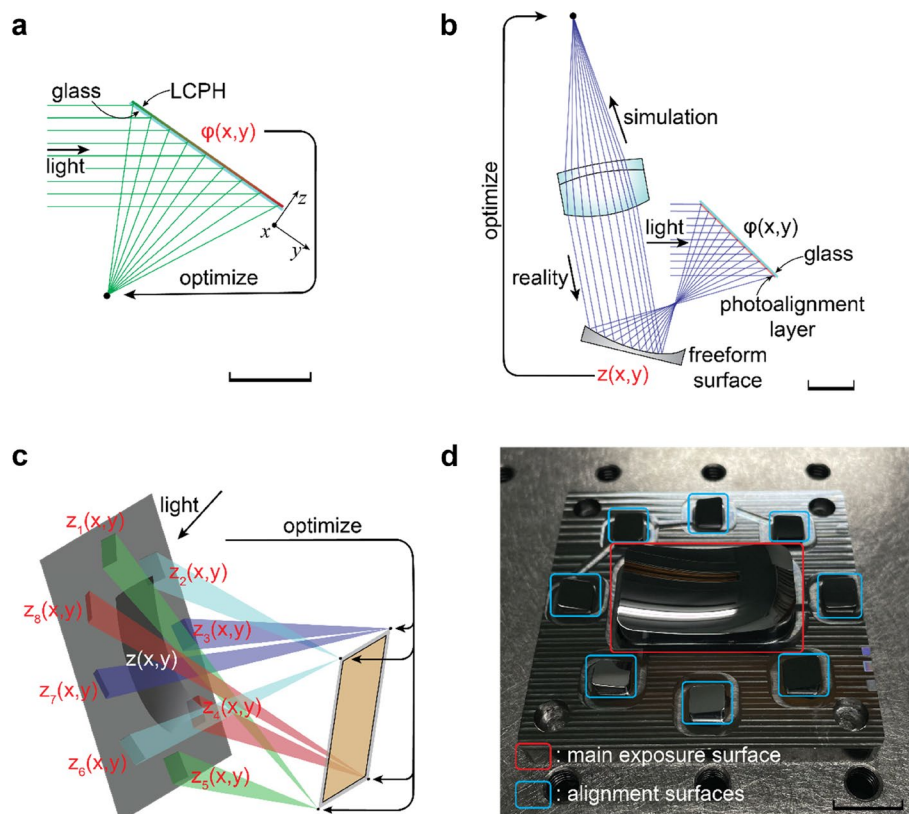


**Fig. 2** Design procedure of freeform surface. **a** Illustration of the optimization process of wavefront function  $\varphi(x, y)$  for the DOE to focus the obliquely incident light into a point. **b** Sketch of the optimization of freeform surface for a point-to-point optical imaging. The direction of light on the left portion is reversed in the actual recording process. **c** Schematic diagram of the optimization of eight peripheral surfaces to focus obliquely incident light into four points around the sample. **d** Photo of the fabricated optical surface with main exposure surface and alignment surfaces. All scale bars: 10 mm. a-c are readapted from the rendering results in Code V

$$\varphi(x, y) = \frac{2\pi}{\lambda_D} \left( -\sin\theta_{in}y + \sqrt{x^2 + y^2 + f^2} \right) \quad (2)$$

where  $\lambda_D$  is the display wavelength,  $\theta_{in}$  is the incident angle, and  $f$  is the lens focal length. Still, for the practical implementation in our ray-tracing software (Code V), a  $x$ - $y$  polynomial is adopted. The coefficients are optimized for the focal spot size, which is nearly diffraction-limited (see Supplementary Section S1).

Next, the freeform surface for the interference exposure can be designed. Because the light source in the exposure interferometer is a laser, which has a high degree of collimation. Therefore, the exposure setup can be regarded as a point-to-point imaging system. For convenience, a reflective freeform surface is adopted, which frees us from the need to consider the material's refractive index. The plot of simulation flow-chart is shown in Fig. 2b. The incoming collimated light, after being deflected by the DOE and freeform reflector, is focused by a lens to a point. The lens is diffraction-limited for normally incident light and is fixed in the simulation. Therefore, if the final spot size can be optimized to be diffraction-limited, the freeform reflector can be considered to perfectly produce the wavefront function  $\varphi(x, y)$ . The designed off-axis lens has a size of 32 mm by 24 mm, an off-axis angle of  $55^\circ$  and a focal length of 25 mm, which correspond to a diagonal FoV of  $77^\circ$ . The surface function of freeform reflector  $z(x, y)$  adopts the  $x$ - $y$  polynomial up to the  $10^{\text{th}}$  order with a base conic:

$$z(x, y) = \frac{c(x^2 + y^2)}{1 + \sqrt{1 - (1 + k)c^2(x^2 + y^2)}} + \sum_{i+j \leq 10} C_{ij}x^i y^j \quad (3)$$

where the odd terms of  $x$  are not used due to symmetry. Unfortunately, owing to the large designed FoV, the final spot size ( $\sim 0.03$  mm) does not reach diffraction-limited performance but is still adequate for the use in RSD. Further improvements can be made by adopting a different base function or higher order terms, if a better optical performance is required.

A point worth noting is the light path in our point-to-point imaging system slightly differs from the actual recording process. To illustrate this, the grating  $k$ -vector on the upper region of DOE in Fig. 2b would be small if it is reflection-type because the diffraction angle is small. But if the DOE is recorded using this setup, the grating  $k$ -vector would be large because the relative angle between two rays is large (notice the direction of one ray is reversed). To resolve this problem, we set the DOE here as transmissive-type and reverse the sign of wavefront function  $\varphi(x, y)$  (see Supplementary Section S1).

The design procedure is theoretically completed after the optimization of main freeform reflector. However, in the actual setup of interferometer, how to precisely place the freeform reflector as designed is a non-trivial issue. In principle, a customized stage can be fabricated to hold the freeform reflector and sample in the designed locations. But that would add extra cost and complexity to the system and prohibits further adjustments. Here, we propose an alignment method based on eight peripheral freeform reflectors. As shown in Fig. 2c, the eight reflectors focus the incoming light to four points near the boundary of sample. The same surface function in



Eq. (3) is adopted for  $z_1(x, y)$  to  $z_8(x, y)$ , except only the polynomial up to 3<sup>rd</sup> order is needed to reach a diffraction-limited performance thanks to the small size of alignment reflectors. A photo of the fabricated sample is shown in Fig. 2d. More details of freeform surface simulation can be found in Supplementary Section S1 and Data 1.

### Inkjet printing

Previous works on printing liquid crystal are mainly based on high-temperature direct ink writing of the solvent-free liquid crystal polymer [29, 30]. The fabricated liquid crystal elastomers normally do not exhibit self-assembly property and therefore cannot be used to form LCPHs. On the other hand, inkjet printing is a convenient method of depositing material [31] and has been widely applied to pattern materials like organic thin film transistors [32], organic light emitting diodes [33] and quantum dots [34]. Lately, a Bragg mirror has been demonstrated using multilayer inkjet printing [35], indicating the potential of inkjet printing to fabricate high-quality optical elements. This solvent-based technique is compatible with the formation mechanism of self-assembled liquid crystal structure and is therefore most ideal for the fabrication of LCPH.

Before going through the design and fabrication details of inkjet-printed LCPH, let us firstly explain why the local variation of deposited liquid crystal is necessary. In a full-color RSD, RGB lasers are incident on the DOE. For the green DOE, if the red and blue lasers are also diffracted, crosstalk stray lights would be formed (Fig. 3a), which greatly compromises the image quality. For a LCPH with uniform chiral pitch and thickness distribution, the crosstalk can only be suppressed in a very limited region of DOE. To illustrate this, the diffraction efficiencies in different regions of a DOE with a CLC pitch of 352 nm and a thickness of 1050 nm are calculated as shown in Fig. 3b. The laser wavelengths of the display engine in this work are 450 nm, 524 nm and 642 nm. For the central region, the diffractions for red and blue are well suppressed. However, the Bragg band red/blue shifts for left/right regions, causing a significantly higher diffraction efficiency for the red and blue lasers.

In order for the red and blue lasers to fall exactly in the adjacent valleys of the green peak, both CLC pitch and film thickness need to be locally adjusted. The variation of CLC pitch results in the overall shifting of Bragg band, while the change in film thickness widens or narrows the gap between two valleys. The brute-force calculation is performed for the optimum CLC pitch and film thickness in every spatial point of DOE, by going through all possible pitch-thickness combinations with a step size. The results are shown in Fig. 3c, d. Notice only the upper portion in  $x$  direction is calculated due to symmetry. Both the pitch and thickness mainly vary in  $y$  direction owing to the large off-axis angle. With the pitch and thickness distribution maps, the next step is to realize them with inkjet printing.

The Sonoplot printer adopted in this work uses a piezoelectric driven inkjet nozzle that dispenses the ink by a contact plotting approach. The printing mechanism differs from the common drop-on-demand (DOD) inkjet printer that ejects ink drops from the printhead. However, this type of line-drawing printing method is more similar to the commonly adopted spin-coating technique and serves as a good starting point to study the inkjet printing of LCPH. The photo of printing process is shown in Fig. 3e, where a well-defined line shape can be observed in the printing trajectory. The continuous area

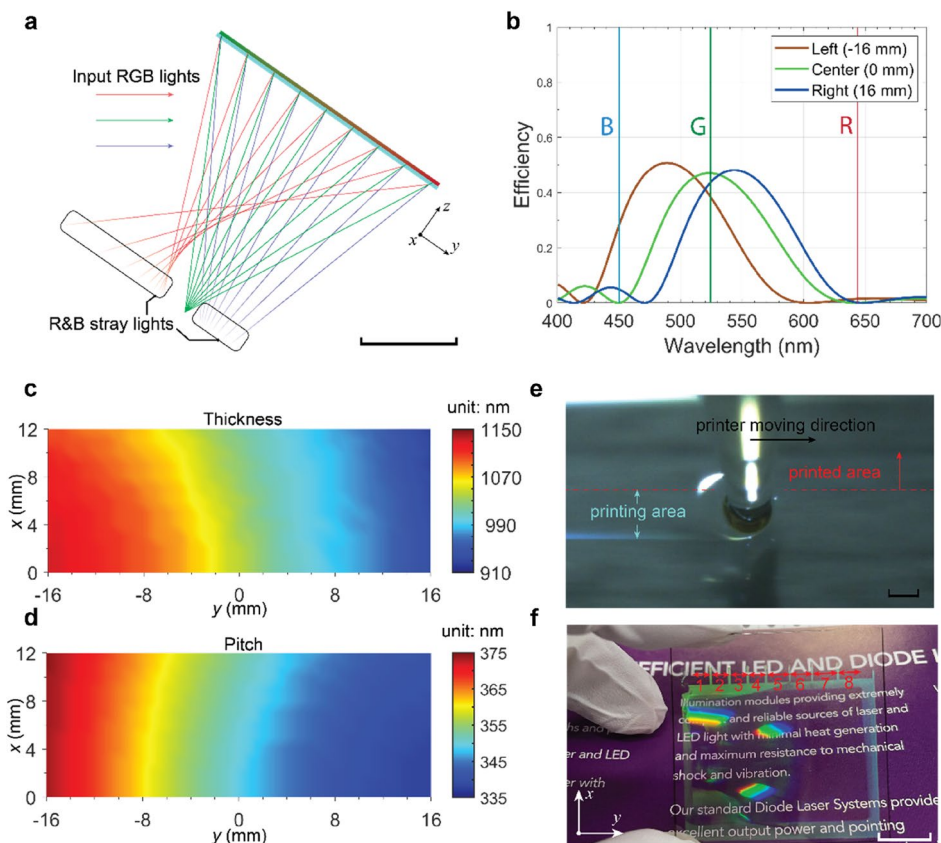


**Fig. 3** Analysis and optimization of inkjet printing process. **a** Schematic illustration of color crosstalk and resulted stray lights (readapted from Code V, scale bar: 10 mm). **b** Simulated diffraction efficiencies in left, center and right regions of a green DOE with uniform pitch and thickness distribution. The wavelengths of RGB lasers in display engine are represented by the colored vertical lines. Optimized distribution of **c** thickness and **d** pitch. **e** Captured image of the printing process. Scale bar: 100  $\mu\text{m}$  **f** Photo of the green DOE sample with eight sections noted by the numbered arrows. Scale bar: 10 mm

is achieved by drawing adjacent lines that merge together (see Supplementary Movie 1). Although in theory multiple parallelly placed printheads can conveniently mix different types of ink at controlled ratios in the printing process, unfortunately only the printer with a single printhead is available from Sonoplot. Therefore, we achieve the local pitch and thickness variation by changing the ink after finishing each subregion. The lens region is sectioned into eight subregions in  $y$  direction (Fig. 3f), in each subregion, the pitch and thickness values are the averaged results from Fig. 3c, d. To make sure the ink loading and unloading processes do not disturb the printed regions, the first and last drawing lines in each printing region are intentionally made longer than others, which is shown in Fig. 3f. The first and last regions also include some redundant area to promise the full cover of target region. In theory, more sections lead to a higher-resolution modulation and hence a weaker crosstalk. The scheme used in this work is the result of balancing fabrication complexity and final performance. It is only for the proof-of-concept purpose and shall not be regarded as the limitation of the inkjet printing technique itself.

A major issue in inkjet printing is the film non-uniformity caused by the so-called coffee ring effect [36]. The coffee ring effect originates from the capillary flows that



transport solutes to the boundary contact line, where the solvent evaporation rate is higher. For a droplet, the final solute distribution is concentrated on the outer circular boundary, and hence the reason for the name “coffee ring”. In our case, the droplet becomes a line after being drawn by the printhead. The coffee ring effect therefore leads to line-shaped non-uniformities of film (see Supplementary Section S4).

One common method to suppress the coffee ring effect is to induce a reverse Marangoni flow that transports the solute accumulated in the contact line back to the center. To that end, another solvent with a lower (or higher) surface tension and a slower (or faster) evaporation speed is mixed with the original solvent. For a water-based ink, this type of solvent is easy to find due to the abnormally high surface tension of water resulted from the strong hydrogen bonding. However, for the organic solvent used to dissolve liquid crystal reactive mesogen (RM257), which is typically toluene or propylene glycol methyl ether acetate (PGMEA), to find such a solvent to induce a significant Marangoni flow is rather challenging (see Supplementary Section S4). Therefore, we adopt another approach to use 1-methylnaphthalene as the solvent, which manifests a high viscosity and a slow evaporation rate. The resultant film exhibits an excellent uniformity, as shown in Fig. 3e and Supplementary Section S4.

## Results

Figure 4a-c shows the measured efficiency spectra of fabricated off-axis lenses for blue, green, and red samples, respectively. For each sample, three measurements are performed in the left, center, and right regions of the lens. For each sample, it can be seen that the other two wavelengths fall in the valleys of Bragg band in all three regions, while the desired wavelength is in the high-efficiency regime. In the meantime, the diffraction efficiencies of the desired wavelength in three regions have

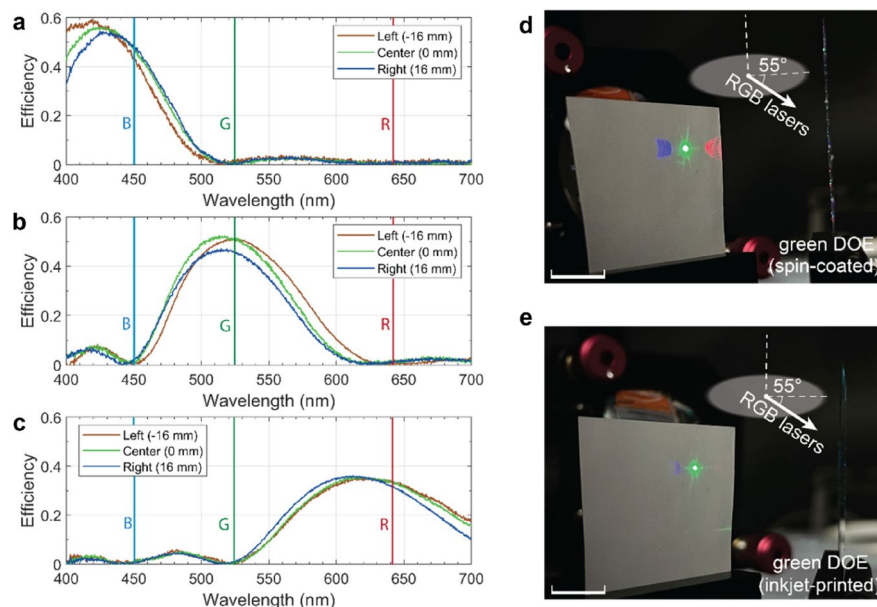


**Fig. 4** Characterization of fabricated DOE samples. Measured diffraction efficiencies of left, center and right regions of **a** blue sample, **b** green sample and **c** red sample. Captured images of the diffracted RGB laser lights of **d** the sample with spin-coating method and **e** the inkjet-printed sample. Scale bars: 10 mm

a small variation. Although the variation does not significantly influence the image performance of RSDs, to eliminate it is possible by further adjusting the liquid crystal birefringence through mixing different compounds together.

To better illustrate the improvement of crosstalk using inkjet printing technique, we fabricated another green DOE with traditional spin-coating method. With RGB laser beams obliquely incident on the sample, the stray lights are clearly observable (Fig. 4d). The ratio between intensities of stray light and input light is measured to be 4.5% for blue and 3.1% for red. On the other hand, the stray lights of inkjet-printed green DOE sample are significantly suppressed (Fig. 4e). The stray light ratio in this case is measured to be 0.51% for blue and 0.48% for red, which corresponds to a suppression of 8.4 times for blue and 6.5 times for red.

The full-color RSD setup is shown in Fig. 5a. The RGB DOEs are manually stacked together to form the full-color combiner. In the stacking process, the relative positions of RGB DOEs are adjusted so that their focal spots are overlapped to the highest degree possible by hand. Lights from the laser projector are collimated by the lens and incident on the RGB DOEs. The image is captured by an iPhone 8 camera with a pupil size of around 2 mm to mimic a human eye. The FoV of RSD is designed to be  $65^\circ$  by  $51^\circ$ , which coincidentally matches the maximum FoV of our camera, as shown in Fig. 5b. Color breakups can be observed in the peripheral regions. This is mainly due to the misalignment of three DOEs. To correct for the misalignment, the RGB sub-images are pre-shifted in the laser projector with the inherent adjustment program. However, this only promises the perfect match in the central region because the focal points of RGB DOEs still do not perfectly overlap. In theory, a better alignment

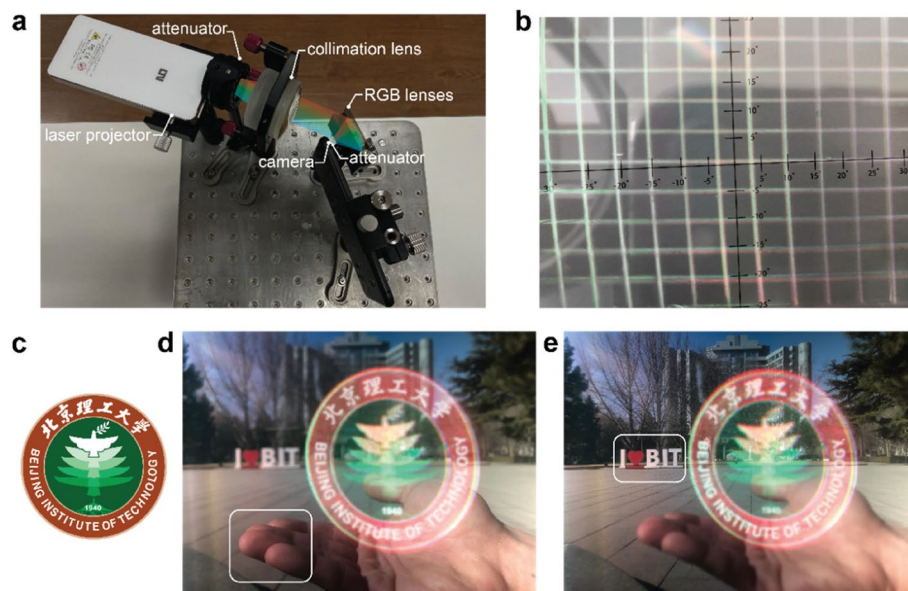


**Fig. 5** Full-color RSD system. **a** Photo of the display system. The light from the laser projector firstly passes an attenuator and gets collimated by a lens. The diffracted light passes another attenuator before being captured by the camera. **b** Captured image of a displayed white grid image in a background with FoV rulers, indicating the maximum FoV of display system. **c** Displayed full-color image. Captured photos of display effect when the camera is focused at **d** near and **e** far distances, as denoted by the white boxes

of RGB DOEs can be achieved with a high-precision mechanical adjuster and fundamentally solve the color breakup issue.

Finally, a full-color image (Fig. 5c) is displayed in an outdoor sunny environment. Two photos are captured when the camera is focused at near (Fig. 5d) and far (Fig. 5e) distances. It can be seen the image brightness is high enough to support a good visibility in such a bright ambient background. The high depth of focus attribute of RSD is confirmed by the good resolution of images at both near and far focuses.

## Discussion

The above results demonstrate the local hologram manipulation ability of the proposed full degree-of-freedom polarization hologram in terms of wavefront and material deposition. Still, there is room for improvement in the fabrication details. For example, the basic function of freeform surface can be further optimized for a higher optical performance. The light intensity distribution on the sample mismatches with the original one, after the modulation by the freeform reflector. Although it does not affect the final exposure performance, to make the two distributions equal is possible by adding another freeform surface in either path. The photoalignment material can also be improved by, for example, using more humidity-tolerant materials like SD1.

The inkjet printing resolution can be improved by increasing the section numbers, or more favorably, adopting the DOD-type inkjet printer whose resolution can achieve  $\sim 20 \mu\text{m}$  for a 1200 dpi printer. In that case, ink parameters like ink viscosity, surface tension, and droplet size should be carefully optimized to achieve a decent printing performance [35]. Additionally, although not demonstrated in this work, additional degrees-of-freedom can be attained by locally mixing different types of liquid crystal materials, which is commonly adopted to optimize for high-performance liquid crystals [37, 38]. Such a locally varied mixture can achieve, for example, the modulation of birefringence and its dispersion, allowing even higher degrees of design freedom.

## Conclusion

In summary, we propose the concept of full degree-of-freedom polarization hologram. Its design and fabrication procedures are exemplified by building a full-color RSD whose RGB off-axis lens DOEs fully exploit the design freedom to eliminate optical aberrations and color crosstalk. Combined with the inherent advantages like dynamic tunability, polarization selectivity, and large refractive index modulation, the full-freedom LCPH can be applied in virtually any scenario requiring a compact DOE and high design freedom. Typical examples include pancake optics, waveguide displays, light field displays, and holographic imaging systems.

## Methods

### Sample fabrication

The main fabrication procedure is depicted in Fig. 6a. The glass substrate with a thickness of 0.2 mm is firstly cleaned with ethanol, acetone, and isopropyl alcohol. Then it is placed in an air plasma cleaner for 10 min to improve surface wettability. The photoalignment material, brilliant yellow (BY, from Shanghai Bepharma Science & Technology) is dissolved in dimethylformamide with a weight ratio of 1%. All solutions in this work

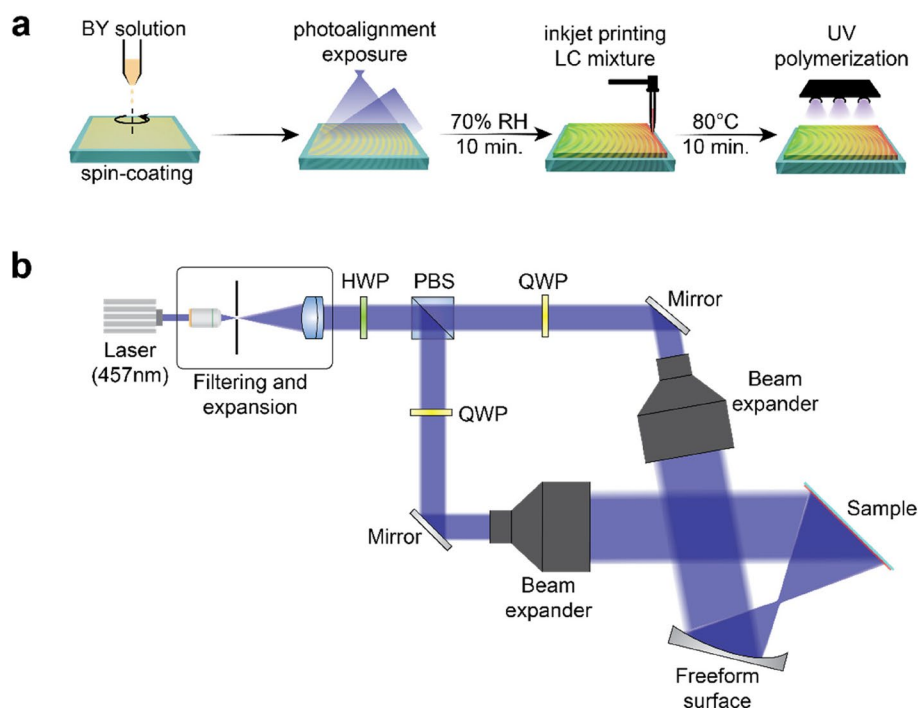


**Fig. 6** Schematic illustration of fabrication procedure. **a** Overall workflow of the fabrication. The sample undergoes steps of spin-coating BY solutions, photoalignment exposure and humidity treatment, inkjet printing LC mixture, heating and UV polymerization. **b** Diagram of exposure interferometer setup. The laser light, after filtering and expansion, is modulated by a HWP and split by a PBS into two beams. Each beam is modulated by a QWP, reflected by a mirror, and expanded by a  $3 \times$  beam expander, before being modulated by the freeform surface (recording beam) or directly reaching the sample (reference beam)

are filtered through  $0.2 \mu\text{m}$  syringe filters before use. The BY solution is spin-coated onto the glass substrate at 500 rpm for 5 s and 3000 rpm for 30 s. The sample is then placed in the interferometer for photoalignment exposure.

The sketch of interferometer is shown in Fig. 6b. The laser (MSL-FN-457-300mW, from Changchun New Industry Photoelectric Technology) has a wavelength of 457 nm and a measured output power of 380 mW. The spatial filtering and beam expansion is performed with a  $20 \times$  objective lens, a  $25\text{-}\mu\text{m}$  pinhole, and a collimation lens with a focal length of 15 cm. The collimated light passes a half-wave plate (HWP) and is split by a polarizing beam splitter (PBS) into two beams. Each beam passes a quarter-wave plate (QWP), a mirror, and a  $3 \times$  beam expander. The position of freeform surface is adjusted so that the peripheral eight alignment mirrors focus the light into four designed points. The HWP is adjusted to vary the light intensity in two paths so that the final intensity on the sample is equal. The QWPs are adjusted so that the final polarization states of beams on the sample are left circularly polarized and right circularly polarized. The final light intensity on the sample is  $5 \text{ mW}/\text{cm}^2$ . The sample is exposed for 5 min, which gives a total dosage of  $1.5 \text{ J}/\text{cm}^2$ .

The humidity in the processes of spin-coating photoalignment material and exposure is kept below 30% RH. After the exposure, the sample is placed in a box with a controlled humidity of 70% RH for 10 min. The purpose of this step is to stabilize the patterned photoalignment layer, as has been pointed out that the post-exposure humidity

treatment can form the J-mesoaggregate of BY molecules that forbids re-alignment [39]. This step is vital because the later inkjet printing is performed in a bright white light environment that would otherwise erase the photoalignment pattern.

The liquid crystal mixture consists of the precursor and the solvent 1- methylnaphthalene. The precursor is composed of the reactive mesogen RM257 (from Henan Alfa Chemical), the chiral dopant R5011 (from NanJing SanJiang Advanced Materials R&D), the photoinitiator Irgacure 651 (from Meryer Shanghai Chemical Technology) and surfactant Zonyl 8857A (from DuPont). The reactive mesogen is a type of polymerizable liquid crystalline material under UV light exposure with the assist of a photoinitiator. The chiral dopant, with a helical twisting power of  $130 \mu\text{m}^{-1}$ , induces the CLC state with a helical pitch according to the following equation:

$$HTP = \frac{1}{c \cdot p} \quad (4)$$

where  $c$  is the concentration of chiral dopant and  $p$  is the helical pitch (rotating from 0 to  $2\pi$ ). The surfactant is used to improve the film quality by cancelling the homeotropic anchoring force at the interface between liquid crystal and air. The concentrations of Irgacure 651 and surfactant are fixed to be 5% and 0.025%. The concentration of chiral dopant and the weight ratio between precursor and solvent are adjusted in each printing subregion for varied pitch and thickness (see Supplementary Section S4).

The inkjet printer (Microplotter II from Sonoplot) is equipped with an 80- $\mu\text{m}$  printhead. The spacing between adjacent lines is 175  $\mu\text{m}$ . In the printing process, the moving speed of printhead is 8 mm/s and the applied voltage is 0.3 V. After printing each subregion, the printhead is rinsed using PGMEA for 2 cycles before loading the new ink.

After the printing process, the sample is placed on a hot plate (80 °C) for 10 min for complete evaporation of solvent. Then, it is placed under a UV lamp (365 nm) for polymerization with an exposure dosage of 114 J/cm<sup>2</sup> (127 mW/cm<sup>2</sup> for 15 min). Notice the dosage is significantly higher than required for pure polymerization ( $\sim 15 \text{ J/cm}^2$ ). The purpose of over-exposure is indeed to remove the yellowish appearance of sample from the BY layer by, presumably, damaging the BY molecules or realigning it vertically.

### Simulation

All the calculations of diffraction efficiencies are performed using rigorous coupled wave analysis [40, 41]. In the calculation, the birefringence dispersion of RM257 is considered using the following formula [42]:

$$\Delta n = G \frac{\lambda^2 \lambda^{*2}}{\lambda^2 - \lambda^{*2}} \quad (5)$$

where  $\Delta n$  is the birefringence,  $G$  is the proportionality constant,  $\lambda^*$  is the mean resonance wavelength, and  $\lambda$  is the wavelength. From fittings, we find  $G = 2.148 \times 10^{-6} \text{ nm}^{-2}$  and  $\lambda^* = 222.4 \text{ nm}$ .

For the optimization of pitch and thickness distribution, the step sizes for pitch and thickness are 1 nm and 5 nm. The upper half lens region (32 mm by 12 mm) is sectioned into a



grid with a unit size of 1 mm by 1 mm. In each grid point, the target function, efficiency sum of two other wavelengths, is minimized by going through all pitch and thickness values.

### Measurements and display system

For the measurement of diffraction efficiency, the transmittance spectrum is firstly measured using a spectrometer (SE1040-025-VNIR from DHC) equipped with a halogen light source. The diffraction efficiency is then obtained by subtracting one by the transmittance spectrum.

The display engine is a laser beam scanning projector (from ViewSmart) that scans three RGB lasers with micro-electro-mechanical system (MEMS) mirrors. The output laser light is collimated by a lens with focal length of 6 cm. The attenuators in Fig. 5a are dual polarizers with adjustable attenuation. The attenuator next to the laser projector is used to decrease the display image brightness that would otherwise make the photo overexposed. The attenuator in front of the camera is to darken the environment and image simultaneously to increase the camera exposure time. Because the display image is generated in a scanning manner, the camera would only capture features of the image if the exposure time is too short.

### Supplementary Information

The online version contains supplementary material available at <https://doi.org/10.1186/s43074-023-00111-6>.

**Additional file 1: Section S1.** Details of freeform surface simulation. **Section S2.** Pitch and thickness optimization. **Section S3.** Characterization and analysis of focal spot. **Section S4.** Implementation details of inkjet printing. **Section S5.** Temperature and UV stability tests.

**Additional file 2.**

### Acknowledgements

The authors would like to thank Synopsys for providing the educational license of Code V.

### Authors' contributions

J.X. proposed the concept and carried out the experiments. J.X. and D.C. co-designed the simulation method of freeform surface. H.Z. helped J.X. with the usage and parameter adjustment of inkjet printer. S.-T.W. helped with data analysis and writing the manuscript. Y.W. supervised the project. All authors discussed the results and contributed to the final manuscript.

### Funding

This research is supported by National Key Research and Development Program of China (2021YFB2802100).

### Availability of data and materials

The data that support the findings of this study are available within the article and its supplementary information. All other relevant data are available from the corresponding authors upon request.

### Declarations

#### Ethics approval and consent to participate

Not applicable.

#### Consent for publication

All authors agree with the publication.

#### Competing interests

The authors declare no competing interests.

Received: 18 May 2023 Revised: 15 August 2023 Accepted: 27 September 2023

Published online: 13 October 2023

## References

1. Gabor D. A New microscopic principle. *Nature*. 1948;161:777–8. <https://doi.org/10.1038/161777a0>.
2. Cooke DJ, Ward AA. Reflection-hologram processing for high efficiency in silver-halide emulsions. *Appl Opt*. 1984;23:934–41. <https://doi.org/10.1364/AO.23.000934>.
3. Chang BJ, Leonard CD. Dichromated gelatin for the fabrication of holographic optoelements. *Appl Opt*. 1979;18:2407–17. <https://doi.org/10.1364/AO.18.002407>.
4. Beesley MJ, Castledine JG. The use of photoresist as a holographic recording medium. *Appl Opt*. 1970;9:2720–4. <https://doi.org/10.1364/AO.9.002720>.
5. Hesselink L, et al. Photorefractive materials for nonvolatile volume holographic data storage. *Science*. 1998;282:1089–94. <https://doi.org/10.1126/science.282.5391.1089>.
6. Colburn WS, Haines KA. Volume hologram formation in photopolymer materials. *Appl Opt*. 1971;10:1636–41. <https://doi.org/10.1364/AO.10.001636>.
7. Hariharan P. *Optical Holography: Principles, Techniques and Applications*. 2nd ed. Cambridge: Cambridge University Press; 1996. <https://doi.org/10.1017/CBO9781139174039>.
8. Chang C, Bang K, Wetzstein G, Lee B, Gao L. Toward the next-generation VR/AR optics: a review of holographic near-eye displays from a human-centric perspective. *Optica*. 2020;7:1563–78. <https://doi.org/10.1364/OPTICA.406004>.
9. Chigrinov VG, Kozenkov VM & Kwok HS. *Photoalignment of liquid crystalline materials: physics and applications*. Hoboken: Wiley; 2008. <https://onlinelibrary.wiley.com/doi/book/10.1002/9780470751800>.
10. Schadt M, Seiberle H, Schuster A. Optical patterning of multi-domain liquid-crystal displays with wide viewing angles. *Nature*. 1996;381:212–5. <https://doi.org/10.1038/381212a0>.
11. Xiong J, Wu S-T. Planar liquid crystal polarization optics for augmented reality and virtual reality: from fundamentals to applications. *eLight*. 2021;1:3. <https://doi.org/10.1186/s43593-021-00003-x>.
12. Crawford GP, Eakin JN, Radcliffe MD, Callan-Jones A, Pelcovits RA. Liquid-crystal diffraction gratings using polarization holography alignment techniques. *J Appl Phys*. 2005;98:123102. <https://doi.org/10.1063/1.2146075>.
13. Sarkissian H, Park B, Tabirian N, Zeldovich B. Periodically aligned liquid crystal: potential application for projection displays. *Mol Cryst Liq Cryst*. 2006;451:1–19. <https://doi.org/10.1080/154214090959957>.
14. Kobashi J, Yoshida H, Ozaki M. Planar optics with patterned chiral liquid crystals. *Nat Photonics*. 2016;10:389–92. <https://doi.org/10.1038/nphoton.2016.66>.
15. Barboza R, Bortolozzo U, Clerc MG, Residori S. Berry phase of light under Bragg reflection by chiral liquid-crystal media. *Phys Rev Lett*. 2016;117:053903. <https://doi.org/10.1103/PhysRevLett.117.053903>.
16. Lee YH, He Z, Wu ST. Optical properties of reflective liquid crystal polarization volume gratings. *J Opt Soc Am*. 2019;B36:D9–12. <https://doi.org/10.1364/JOSAB.36.0000D9>.
17. Xiong J, Chen R, Wu S-T. Device simulation of liquid crystal polarization gratings. *Opt Express*. 2019;27:18102–12. <https://doi.org/10.1364/OE.27.018102>.
18. Wu H, et al. Arbitrary photo-patterning in liquid crystal alignments using DMD based lithography system. *Opt Express*. 2012;20:16684–9. <https://doi.org/10.1364/OE.20.016684>.
19. Kim J, et al. Fabrication of ideal geometric-phase holograms with arbitrary wavefronts. *Optica*. 2015;2:958–64. <https://doi.org/10.1364/OPTICA.2.000958>.
20. Cakmakci O, Rolland J. Head-worn displays: a review. *J Disp Technol*. 2006;2:199–216. <https://doi.org/10.1109/JDT.2006.879846>.
21. Jang C, et al. Retinal 3D: augmented reality near-eye display via pupil-tracked light field projection on retina. *ACM Trans Graph*. 2017;36:190. <https://doi.org/10.1145/3130800.3130889>.
22. Maimone A, Georgiou A, Kollin JS. Holographic near-eye displays for virtual and augmented reality. *ACM Trans Graph*. 2017;36:85. <https://doi.org/10.1145/3072959.3073624>.
23. Park JH, Kim SB. Optical see-through holographic near-eye display with eyebox steering and depth of field control. *Opt Express*. 2018;26:27076–88. <https://doi.org/10.1364/OE.26.027076>.
24. Xiong J, Li Y, Li K, Wu S-T. Aberration-free pupil steerable Maxwellian display for augmented reality with cholesteric liquid crystal holographic lenses. *Opt Lett*. 2021;46:1760–3. <https://doi.org/10.1364/OL.422559>.
25. Yang Q, Li Y, Ding Y & Wu ST. Compact Foveated AR Displays with Polarization Selective Planar Lenses. *ACS Appl Opt Mater*. 2023. <https://doi.org/10.1021/acsaom.2c00203>
26. Rolland JP, et al. Freeform optics for imaging. *Optica*. 2021;8:161–76. <https://doi.org/10.1364/OPTICA.413762>.
27. Jang C, et al. Design and fabrication of freeform holographic optical elements. *ACM Trans Graph*. 2020;39:1–15.
28. Yang T, Wang Y, Ni D, Cheng D, Wang Y. Design of off-axis reflective imaging systems based on freeform holographic elements. *Opt Express*. 2022;30:20117–34. <https://doi.org/10.1364/OE.460351>.
29. Kotikian A, Truby RL, Boley JW, White TJ, Lewis JA. 3D Printing of liquid crystal elastomeric actuators with spatially programmed nematic order. *Adv Mater*. 2018;30:1706164. <https://doi.org/10.1002/adma.201706164>.
30. Gantenbein S, et al. Three-dimensional printing of hierarchical liquid-crystal-polymer structures. *Nature*. 2018;561:226–30. <https://doi.org/10.1038/s41586-018-0474-7>.
31. Wu L, Dong Z, Li F, Zhou H, Song Y. Emerging progress of inkjet technology in printing optical materials. *Adv Opt Mater*. 2016;4:1915–32. <https://doi.org/10.1002/adom.201600466>.
32. Minemawari H, et al. Inkjet printing of single-crystal films. *Nature*. 2011;475:364–7. <https://doi.org/10.1038/nature10313>.
33. Gorter H, et al. Toward inkjet printing of small molecule organic light emitting diodes. *Thin Solid Films*. 2013;532:11–5. <https://doi.org/10.1016/j.tsf.2013.01.041>.
34. Liu Z, et al. Micro-light-emitting diodes with quantum dots in display technology. *Light Sci Appl*. 2020;9:83. <https://doi.org/10.1038/s41377-020-0268-1>.
35. Zhang Q, et al. Fabrication of Bragg mirrors by multilayer inkjet printing. *Adv Mater*. 2022;34:2201348. <https://doi.org/10.1002/adma.202201348>.
36. Hoath SD. *Fundamentals of Inkjet Printing: The Science of Inkjet and Droplets*. Hoboken: Wiley; 2016. <https://onlinelibrary.wiley.com/doi/book/10.1002/9783527684724>.
37. Dąbrowski R, Kula P, Herman J. High Birefringence Liquid Crystals. *Crystals*. 2013;3:443–82.

38. Dąbrowski R, et al. Low viscosity, high birefringence liquid crystalline compounds and mixtures. *Opto-Electron Rev.* 2007;15:47–51. <https://doi.org/10.2478/s11772-006-0055-4>.
39. Shi Y, et al. High Photoinduced ordering and controllable photostability of hydrophilic Azobenzene material based on relative humidity. *Langmuir.* 2018;34:4465–72. <https://doi.org/10.1021/acs.langmuir.8b00039>.
40. Xiong J, Wu S-T. Rigorous coupled-wave analysis of liquid crystal polarization gratings. *Opt Express.* 2020;28:35960–71. <https://doi.org/10.1364/OE.410271>.
41. Moharam MG, Gaylord TK. Rigorous coupled-wave analysis of planar-grating diffraction. *J Opt Soc Am.* 1981;71:811–8. <https://doi.org/10.1364/JOSA.71.000811>.
42. Wu S-T. Birefringence dispersions of liquid crystals. *Phys Rev.* 1986;A 33:1270–4. <https://doi.org/10.1103/PhysRevA.33.1270>.

### Publisher's Note

Springer Nature remains neutral with regard to jurisdictional claims in published maps and institutional affiliations.

**Submit your manuscript to a SpringerOpen<sup>®</sup> journal and benefit from:**

- ▶ Convenient online submission
- ▶ Rigorous peer review
- ▶ Open access: articles freely available online
- ▶ High visibility within the field
- ▶ Retaining the copyright to your article

---

Submit your next manuscript at ▶ [springeropen.com](https://www.springeropen.com)

---